Simulations of MJO Propagation across the Maritime Continent: Impacts of SST Feedback

JIESHUN ZHU

Climate Prediction Center, NOAA/NWS/NCEP, and Earth System Science Interdisciplinary Center, University of Maryland, College Park, College Park, Maryland

WANQIU WANG AND ARUN KUMAR

Climate Prediction Center, NOAA/NWS/NCEP, College Park, Maryland

(Manuscript received 10 May 2016, in final form 8 November 2016)

ABSTRACT

The observed Madden–Julian oscillation (MJO) tends to propagate eastward across the Maritime Continent from the eastern equatorial Indian Ocean to the western Pacific. However, numerical simulations present different levels of fidelity in representing the propagation, especially for the tropical convection associated with the MJO. This study conducts a series of coupled simulations using the NCEP CFSv2 to explore the impacts of SST feedback and convection parameterization on the propagation simulations. First, two simulations differing in the model horizontal resolutions are conducted. The MJO propagation in these two simulations is found generally insensitive to the resolution change. Further, based on the CFSv2 with a lower resolution, two additional experiments are performed with model SSTs nudged to climatologies with different time scales representing different air–sea coupling strength. It is demonstrated that weakening the air–sea coupling strength significantly degrades the MJO propagation simulation, suggesting the critical role of SST feedback in maintaining MJO propagation. Last, the sensitivity to convection parameterization is explored by comparing two simulations with different convection parameterization schemes. Analyses of these simulations indicate that including air–sea coupling alone in a dynamical model does not result in realistic maintenance of the MJO eastward propagation without the development of favorable SST conditions in the western Pacific. In both observations and one simulation with realistic MJO propagations, the preconditioning of SSTs is strongly affected by surface latent heat fluxes that are modulated by surface wind anomalies in both zonal and meridional directions. The diagnostics highlight the critical contribution from meridional winds in wind speed variations, which has been neglected in most MJO studies.

1. Introduction

The Madden–Julian oscillation (MJO) is the primary mode of tropical intraseasonal climate variability in the boreal winter and spring (Madden and Julian 1971; Zhang 2005). It manifests as a planetary-scale system with organized multiscale convection and large-scale circulation and is featured by its eastward propagation along the equator. During a typical MJO event, a positive convection/rainfall anomaly develops over the western Indian Ocean, while convection tends to be suppressed farther east over the western Pacific. Over the course of the following 30–60 days, the enhanced convective anomaly in the Indian Ocean intensifies and propagates across the Maritime Continent and the western-central Pacific Ocean.

The simulation of the MJO has become a benchmark test for the performance of climate models in the tropics. Although many general circulation models (GCMs) have improved representations of the MJO, many shortcomings still remain, for example, in the simulation of the period, amplitude, seasonality, and geographical dependence of the MJO (Slingo et al. 1996; Lin et al. 2006; Hung et al. 2013; Jiang et al. 2015). A common shortcoming in many GCMs is that the eastward propagation of convection from the Indian Ocean into the western Pacific (i.e., the propagation across the Maritime Continent) remains often poorly represented with standing oscillations of convective activity over the Indian Ocean or western Pacific (Jiang et al. 2015). The model bias in the propagation of MJO across the

Corresponding author e-mail: Dr. Jieshun Zhu, jieshun.zhu@noaa.gov

DOI: 10.1175/JCLI-D-16-0367.1

Maritime Continent has been one of motivations for the Year of the Maritime Continent (YMC; http://www.bmkg.go.id/ymc/default.bmkg), an international project with an overarching goal of ''observing the weather-climate system of the Earth's largest archipelago to improve understanding and prediction of its local variability and global impact.''

Simulations of the MJO have been found sensitive to model configurations. Among various factors, convection parameterization is considered the foremost (Zhang et al. 2006). Studies have suggested that the simulated MJO strongly depends on the criteria for the onset of the convection, for example, the convection entrainment rate and critical relative humidity (Tokioka et al. 1988; Wang and Schlesinger 1999; Zhang and Mu 2005; Bechtold et al. 2008; Lin et al. 2008). Meanwhile, application of different convection schemes may also result in different levels of fidelity in representing the MJO. For example, based on the NCEP Climate Forecast System, version 1 (CFSv1), Seo and Wang (2010) performed a series of experiments to explore the impacts of various factors on the simulation of the MJO. They found that the simulation strongly depended on the convection parameterization, and the use of the relaxed Arakawa–Schubert (RAS) cumulus parameterization of Moorthi and Suarez (1999) produced a significantly better representation of the MJO with more realistic periodicity, spectral power, and eastward propagation than simplified Arakawa–Schubert (SAS) cumulus parameterization (Pan and Wu 1995). The superiority of RAS over SAS in the MJO simulations was also achieved by Wang et al. (2015) using the atmospheric component of CFSv2 (Saha et al. 2014). Meanwhile, Bechtold et al. (2008) also showed that improvements to convection and diffusion were responsible for an improved representation of the MJO in the ECMWF Integrated Forecast System.

Another process that affects the MJO is the representation of air–sea interaction. Observational diagnoses have shown coherent variations in surface heat fluxes, SST, and convection associated with the MJO (e.g., Krishnamurti et al. 1988; Shinoda et al. 1998; Woolnough et al. 2000; Kumar et al. 2013). Many numerical studies also noted improved MJO simulations when an atmosphere-only GCM (AGCM) is coupled to an ocean model (e.g., Flatau et al. 1997; Waliser et al. 1999; Kemball-Cook et al. 2002; Inness et al. 2003; Zhang et al. 2006), confirming the role of ocean feedbacks in the MJO life cycle. Moreover, studies also found that the inclusion of air–sea coupling could extend the MJO predictability and enhance prediction skill of the tropical intraseasonal oscillation (e.g., Vitart et al. 2007; Fu et al. 2008; Pegion and Kirtman 2008; Shelly et al. 2014). Prominent ocean–atmosphere coupled processes are also simulated during the propagation of MJO events with high prediction skill in the ECMWF ensemble prediction system (Kim et al. 2016).

The role of SST feedback is also highlighted in many MJO theories, for example, the air–sea convective intraseasonal interaction (ASCII) mechanism that was proposed by Flatau et al. (1997) based on observational analysis and examined by their simplified experiments. The ASCII mechanism relies on the climatological low-level westerly wind in the region through which the convection propagates. Particularly, the zonal wind anomalies associated with the inflow into the convective region strengthen or weaken the surface winds, which reduce or enhance the latent heat flux (LHF) at the ocean surface. Further, variations in solar shortwave radiation flux (SWF) at the surface associated with MJO-related changes in cloudiness also occur. The combination of these flux variations can induce SST anomalies to the east and west of the convective region. The zonal SST gradient causes zonal changes in surface moist static energy and provides surface forcing, which induces the convection to move toward the east.

Coupling an AGCM to an interactive ocean model, however, is not a panacea for problems of simulating the MJO in an uncoupled GCM (Hendon 2000). In fact, many coupled atmosphere–ocean models still exhibit systematic errors in both MJO simulations (Lin et al. 2006; Hung et al. 2013; Jiang et al. 2015) and predictions (Wang et al. 2014). There are investigations suggesting that other aspects of the GCM configuration, such as the treatment of cumulus convection and model resolution, could also affect the response of the MJO to air–sea interactions (e.g., Seo and Wang 2010; Crueger et al. 2013). For example, Crueger et al. (2013), based on ECHAM6, found that the effect of air–sea coupling on the MJO propagation simulations is more evident at high resolution. Furthermore, only a small subset of experiments demonstrated that coupling could even degrade the representation of the MJO in coupled climate simulations (Hendon 2000; Liess et al. 2004). Studies are also devoted to understanding reasons for degradation in the MJO simulation, and it has been mostly linked to biases in the CGCM mean state (e.g., Hendon 2000; Liess et al. 2004; Zhang 2005). For instance, Hendon (2000) attributed the degradation to errors in the basic state climatology of the model (particularly the lack of mean surface westerlies across much of the warm pool) and too-weak latent heat flux anomalies.

Inness and Slingo (2003), based on the Hadley Centre Coupled Model, version 3 (HadCM3), found that, while coupling improved the eastward propagation of

convection across the Indian Ocean, it could not make it propagate farther eastward and into the western Pacific. Inness et al. (2003) further demonstrated that it was also errors in the low-level zonal wind component in the western Pacific that prevented the MJO from propagating into the region, a result which was confirmed by their flux-corrected simulations. The two model studies are generally consistent with the ASCII mechanism (Flatau et al. 1997), and they all emphasize the critical role of the low-level zonal winds. On the other hand, in Seo and Wang (2010), the problem of simulating the MJO in CFSv1 with the SAS convection scheme was attributed to the too-low fraction of the stratiform rainfall relative to the total rainfall over the MJO development region.

In general, the effect of air–sea coupling on the MJO simulations could be model dependent, and so is the physical reasoning behind it. Thus, assessment of various factors influencing MJO simulations is required across diverse models. However, as recognized by DeMott et al. (2015), in such studies, the primary attention has been paid to inter-GCM variations in the effects of coupling than to intra-GCM variations related to the model's physical parameterizations and configurations. The purpose of this study is to contribute to the continuing efforts toward understanding problems on the MJO simulations. For this purpose, a series of coupled simulations are conducted based on a single GCM, that is, the NCEP CFSv2 (Saha et al. 2014). These experiments differ in their model configurations, including horizontal resolutions, convection parameterizations, and the strength of SST feedback.

Our focus is on the simulations of MJO propagation across the Maritime Continent. The Maritime Continent has been known as an MJO ''propagation barrier'' for many GCMs, but its role in supporting or hindering the MJO has not been well understood (Inness and Slingo 2006). By diagnosing the experiments, we address the following two questions: (i) is the air–sea interaction (or SST feedback) critical for simulating the eastward propagation of the MJO, and if so, then (ii) what processes are responsible for the development of SST conditions favorable for the MJO propagation across the Maritime Continent? Question (i) is explored by comparing simulations with predicted SSTs nudged to climatological values with different strengths representing different degree of air–sea coupling. For question (ii), we investigate physical processes contributing to SST evolutions in observations and two CFSv2 simulations with contrasting levels of fidelity in simulating the MJO eastward propagation, which results from different convection schemes.

The paper is organized as follows: The model, the experimental design, and the datasets are described in the section 2. The results are presented in section 3, where factors influencing MJO propagation simulations are explored with a focus on the SST feedback. A discussion and conclusions are given in section 4.

2. Models, experiments, and datasets

a. Models

In this study, the NCEP CFSv2 (Saha et al. 2014) is used for a series of MJO simulation experiments. In addition, CFSv2 with a lower resolution (referred to as CFSv2L) is also applied for experiments. The ocean component (the GFDL MOM, version 4) of CFSv2 (and CFSv2L) is configured for the global ocean with a horizontal grid of 0.5° × 0.5° (1° × 1°) poleward of 30°S and 30°N and meridional resolution increasing gradually to 0.25° (0.33°) between 10°S and 10°N. The vertical coordinate is geopotential height (z coordinate) with 40 levels (27 levels in the upper 400 m), with maximum depth of approximately 4.5 km. The atmospheric component of CFSv2 (CFSv2L) has horizontal resolutions at T126 (T62) spectral truncation with 64 vertical levels in a hybrid sigma–pressure coordinate. The two components exchange surface momentum, heat, and freshwater fluxes, as well as SSTs, every 30 (60) minutes in CFSv2 (CFSv2L).

Different from the standard configuration of CFSv2 (Saha et al. 2014), which uses the 2007 version of the NCEP operational Global Forecast System (GFS), the atmospheric component in the two coupled systems used in this study (CFSv2 and CFSv2L) is the 2011 version of the NCEP GFS, but the model physics are configured as in Saha et al. (2014). In this study, the following two convection schemes built into the model are used for experiments.

1) The SAS cumulus convection scheme (Pan and Wu 1995), which was used in Saha et al. (2014), is based on the original Arakawa and Schubert scheme (Arakawa and Schubert 1974) and simplified by Grell (1993) to consider only one cloud instead of a spectrum of clouds. Convection occurs when the cloud work function exceeds a certain threshold. A simple trigger is employed, which requires that the level of free convection must exist and must be within the distance of 150 hPa of the parcel starting level.
2) The RAS cumulus convection scheme, which in the GFS was developed by Moorthi and Suarez (1992, 1999), simplifies the entrainment relation and assumes that the normalized mass flux is a linear function of height rather than being exponential as in the original Arakawa and Shubert scheme. In

TABLE 1. Description of experiments.

Experiment	Model	Convection scheme	SST nudging (restoring time scale)
CFSv2_RAS	CFSv2	RAS	No
CFSv2L_RAS	CFSv2L	RAS	No
CFSv2L_RAS_SST1dy	CFSv2L	RAS	Yes (1 day)
CFSv2L_RAS_SST10dy	CFSv2L	RAS	Yes (10 days)
CFSv2_SAS	CFSv2	SAS	No

addition, rather than requiring that "quasi equilibrium" of the cloud ensemble be achieved each time, the scheme only relaxes the ambient atmospheric state toward equilibrium.

b. Experiments

Based on the two coupled systems (CFSv2 and CFSv2L) with different horizontal resolutions, five simulation experiments are conducted (Table 1). All the five simulations are initialized from the Climate Forecast System Reanalysis (CFSR; Saha et al. 2010) state on 1 January 1980 and run for 25 years. All model diagnoses are based on outputs of the last 20 years.

- The first two simulations are based on CFSv2 and CFSv2L, both using the RAS convection scheme (referred to as CFSv2_RAS and CFSv2L_RAS). The comparison between CFSv2_RAS and CFSv2L_RAS explores the impact of model resolutions on MJO simulations.
- The third and fourth experiments (referred to as CFSv2L_RAS_SST10dy and CFSv2L_RAS_SST1dy) are designed to explore the role of SST feedback by comparing them with CFSv2L_RAS. In the two experiments, all settings are the same as CFSv2L_RAS except that predicted SSTs during integrations are nudged to CFSv2L_RAS climatological SSTs with the seasonal cycle. Nudging to the CFSv2L_RAS SSTs other than the observational counterpart has the advantage of removing the possible influence of differences in the basic state climate associated with coupled model SST biases. The restoring time scales are chosen as 10 days and 1 day for CFSv2L_RAS_SST10dy and CFSv2L_RAS_SST1dy, respectively. The choice of the 10-day time scale for CFSv2L_RAS_SST10dy takes into account the fact that in observations and CGCMs, there are coherent relationships between MJO convection, surface fluxes, and SSTs with a lag of around 10 days (e.g., Woolnough et al. 2000; Kumar et al. 2013; DeMott et al. 2015). The use of the 1-day time scale for CFSv2L_RAS_SST1dy is to compare the impact when the air–sea interaction is essentially removed.
- The fifth simulation is based on CFSv2 and the SAS convection scheme (referred to as CFSv2_SAS). CFSv2_SAS corresponds to the standard version of CFSv2 (Saha et al. 2014). Its comparison with CFSv2_RAS examines the effect of convection schemes on MJO simulations.

c. Analysis method and observations

Anomalies are calculated as departures from seasonal climatology, which is defined as annual mean plus the first four harmonics of long-term average. To focus on the intraseasonal variability, most analyses are based on intraseasonal anomalies obtained by applying 20–100-day bandpass filtering to the raw daily mean anomalies. When evaluating the zonal propagation features of the simulated MJO, lead–lag correlations or regressions are calculated for the 10°S–10°N averaged intraseasonal anomalies with respect to the Indian Ocean precipitation (10°S–10°N, 70°–100°E). To identify the physical factor modulating LHF variations, a simplified bulk formula [i.e., see Eq. (1)] is used to diagnose LHF based on SST, 2-m specific humidity, 10-m velocity, and sea level pressure. In this study, we take surface flux anomalies as being positive into the ocean surface. Thus, a positive LHF anomaly corresponds to a reduction in evaporation from the ocean.

The observational data used for validations include daily SST analyses from the National Centers for Environmental Information (NCEI) using the optimum interpolation (IO) scheme (Reynolds et al. 2007); rainfall estimate from the CPC morphing technique (CMORPH) satellite retrieval (Joyce et al. 2004); and 850-hPa zonal winds (U850), surface SWF, and LHF from the CFSR (Saha et al. 2010). For the LHF calculation based on the simplified bulk formula [i.e., see Eq. (1)], daily SST, 2-m specific humidity, 10-m velocity, and sea level pressure from CFSR are used as well. All the observational diagnoses are based on data during 1998–2014.

3. Results

a. The impact of horizontal resolutions on the MJO simulations

The effect of model resolution on the MJO is explored by comparing CFSv2_RAS with CFSv2L_RAS.

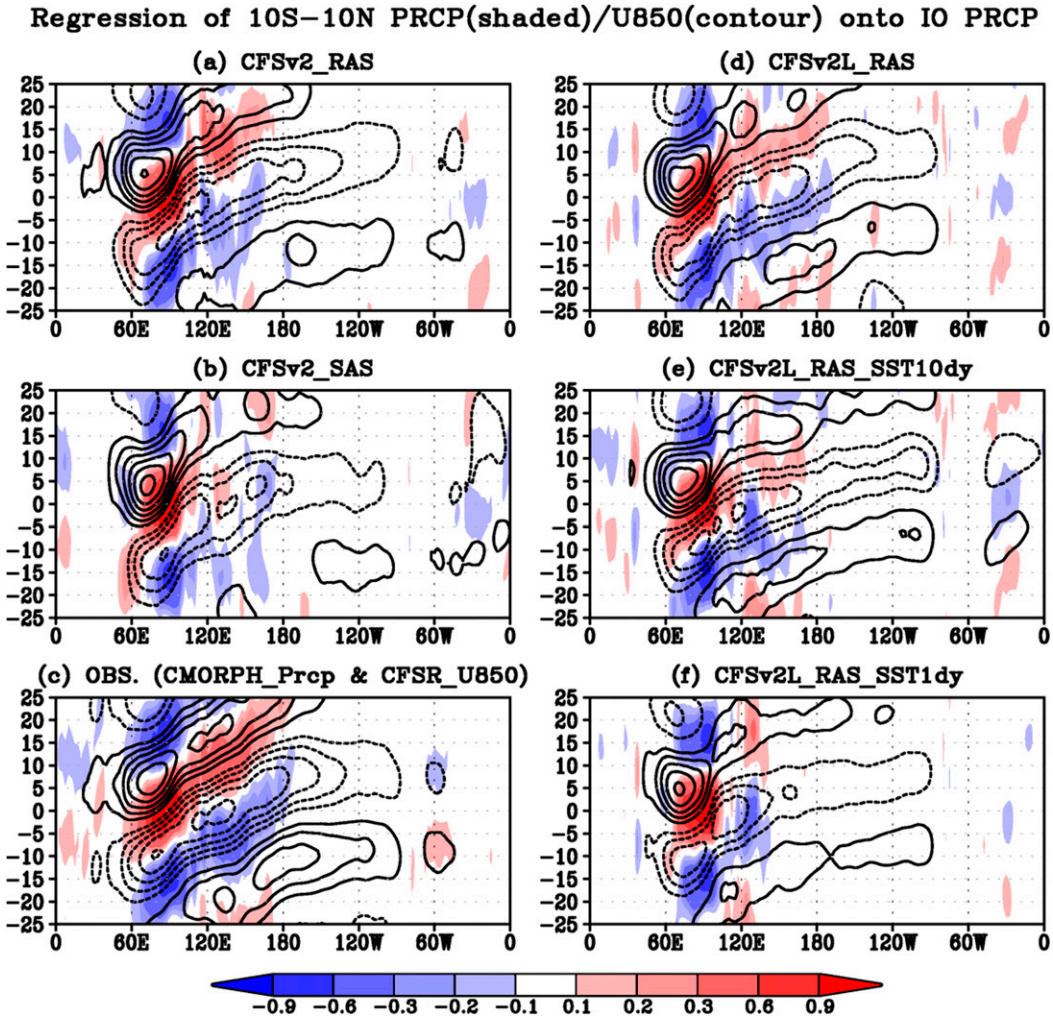

FIG. 1. November–April lag–longitude diagram of 10°S–10°N averaged intraseasonal (20–100-day filtered) precipitation anomalies (color shading) and U850 anomalies [contours; m s^{-1} (mm day^{-1})$^{-1}$] regressed against the Indian Ocean precipitation (10°S–10°N, 70°–100°E) for (a) CFSv2_RAS, (b) CFSv2_SAS, (c) observations (CMORPH precipitation and CFSR U850), (d) CFSv2L_RAS, (e) CFSv2L_RAS_SST10dy, and (f) CFSv2L_RAS_SST1dy. Contour interval is 0.1 m s^{-1} (mm day^{-1})$^{-1}$, with the zero contour omitted.

Investigations about the climatological-mean states between these two simulations suggest that the mean biases in SST, the low-level zonal wind, and precipitation are generally similar over the tropical Indian Ocean and the western Pacific (figures not shown).

For the simulation of the MJO, CFSv2_RAS and CFSv2L_RAS also exhibit the comparable level of fidelity. In terms of spatial distribution of intraseasonal variance (figures not shown), CFSv2_RAS captures some finer structures than CFSv2L_RAS over the Maritime Continent with complex topography, but they are not significantly different on a larger spatial scale. In particular, both models simulate similar and generally realistic variance maps for 850-hPa zonal wind and precipitation featured by large variance over the Indian Ocean and the western Pacific and low variance over the Maritime Continent.

The eastward propagation of the MJO is also simulated at the similar level of fidelity. Figures 1a and 1d show time–longitude diagrams of intraseasonal precipitation anomalies (color shading) and 850-hPa zonal wind anomalies (contours) regressed against the precipitation over the Indian Ocean (10°S–10°N, 70°–100°E) for boreal winter. Similar to their observational counterpart (Fig. 1c), the simulated MJOs propagate eastward across the Eastern Hemisphere at a speed of around 4 m s^{-1}, with the westerly wind anomalies lagging behind positive precipitation anomalies by about

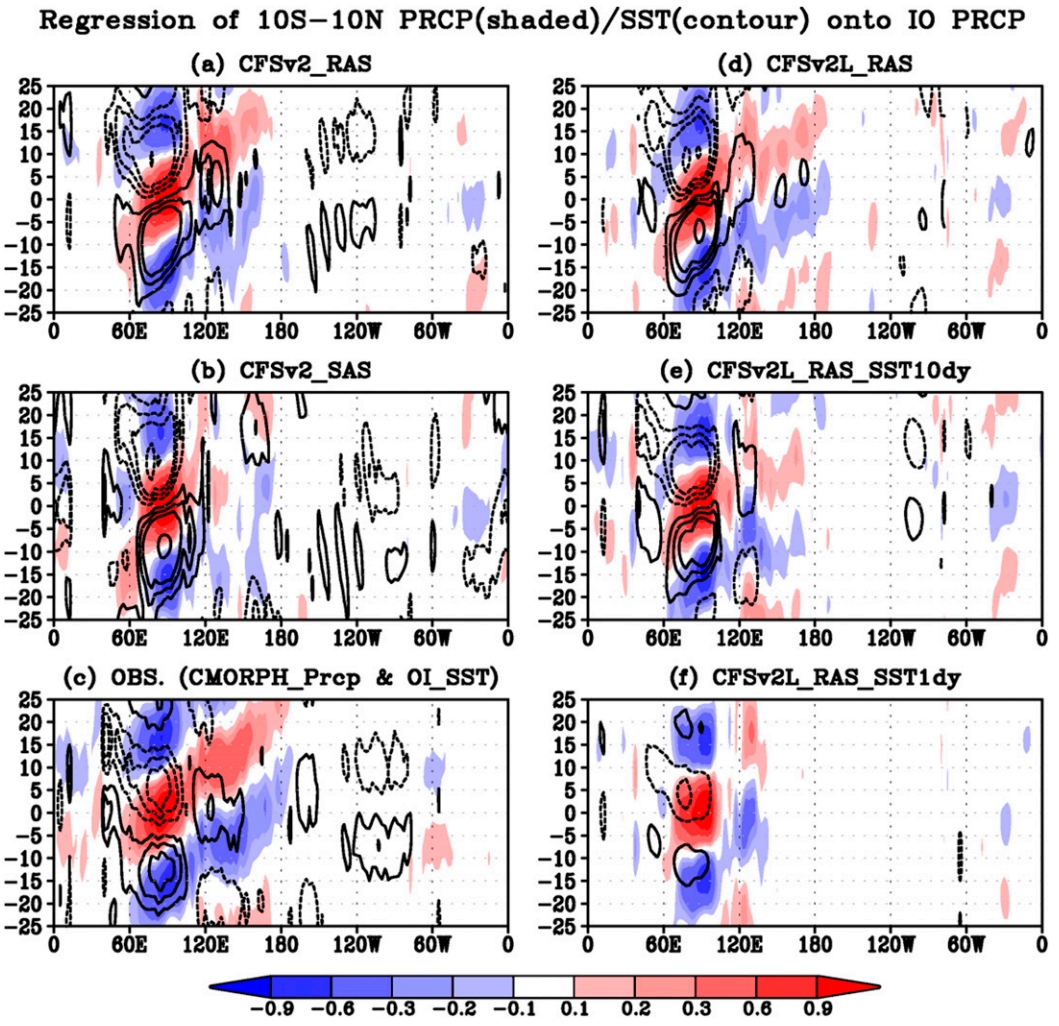

FIG. 2. As in Fig. 1, but for contours for SST anomalies. SST contours are plotted at −0.09°, −0.06°, −0.03°, −0.02°, −0.01°, 0.01°, 0.02°, 0.03°, 0.06°, and 0.09°C (mm day^{-1})$^{-1}$.

5–7 days. In addition, while the precipitation anomalies are generally confined to the Eastern Hemisphere (color shading in Figs. 1a,c,d), the 850-hPa zonal wind anomalies could propagate farther eastward in the Western Hemisphere at a faster speed (contours in Figs. 1a,c,d). It is worthy of highlighting that in contrast to most state-of-the-art models that suffer from the MJO propagation barrier over the Maritime Continent (Jiang et al. 2015), the MJO in CFSv2_RAS and CFSv2L_RAS is able to propagate across the Maritime Continent as in observations. Comparing CFSv2_RAS with CFSv2L_RAS, a discontinuity in convection is more evident at the Maritime Continent in CFSv2_RAS, which might be due to finer orography (Inness and Slingo 2006) or better resolved surface boundary conditions including land fraction and soil and vegetation parameters (Schiemann et al. 2014) at the higher resolutions in CFSv2_RAS.

Accompanying the propagation signal in precipitation anomalies and 850-hPa zonal wind anomalies, intraseasonal anomalies of SST and surface fluxes in observations also exhibit eastward propagation (Figs. 2c, 3c, and 4c), which are captured by CFSv2_RAS (Figs. 2a, 3a, and 4a) and CFSv2L_RAS (Figs. 2d, 3d, and 4d) generally well. The lag–longitude diagrams with SST (contours in Figs. 2a,c,d) show warm SST anomalies in the Indian Ocean prior to the convection and cold SST anomalies after the convection. Associated with the convection in the Indian Ocean, warm SST anomalies appear in the western Pacific. According to the ASCII mechanism (Flatau et al. 1997), the zonal SST gradient could induce the convection to move eastward. The intraseasonal SST anomalies are a response to the air–sea heat flux forcing, as evidenced by a general 1-quadrant-lag relationship between them (figures not shown). Further diagnoses suggest that the surface heat flux

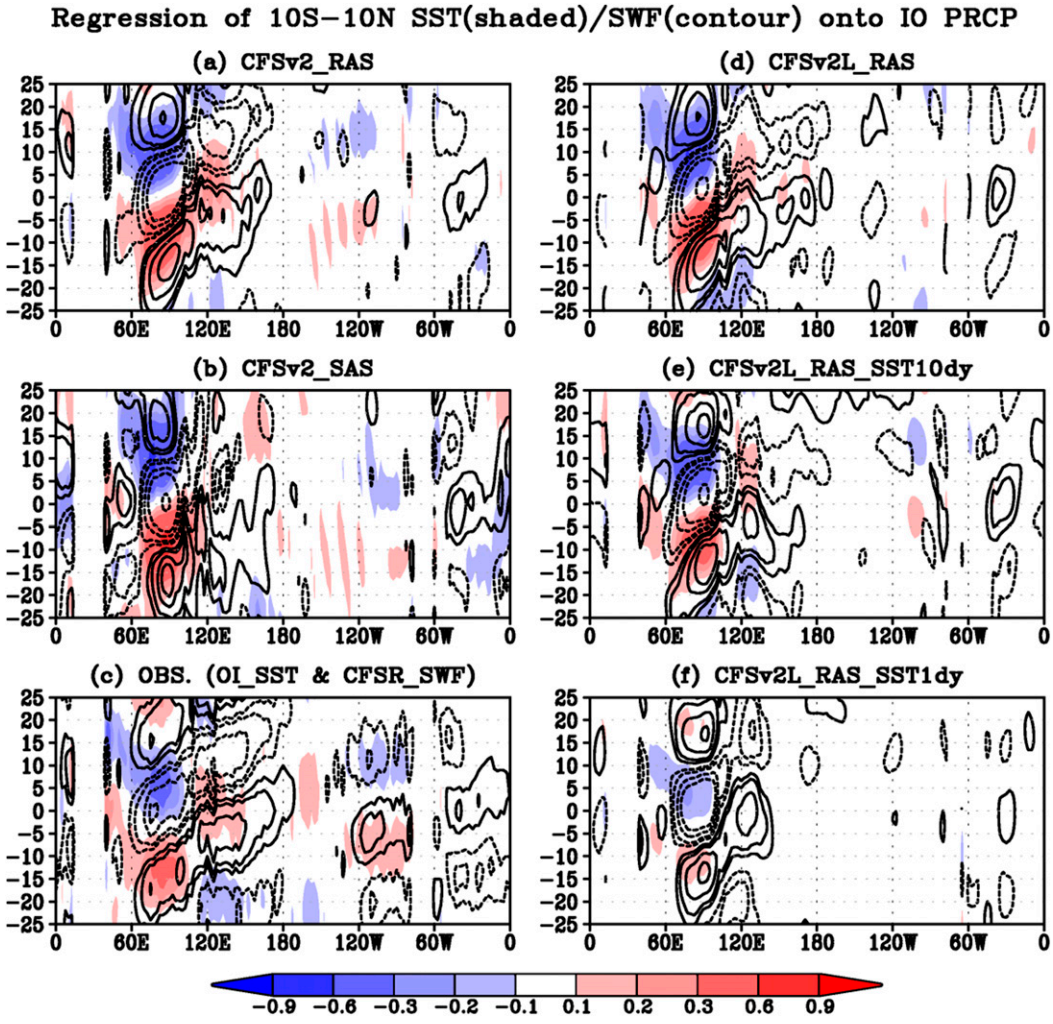

FIG. 3. As in Fig. 1, but for color shading for SST anomalies $[10^{-1}°\text{C (mm day}^{-1})^{-1}]$ and contours for surface net downward SWF anomalies $[\text{W m}^{-2}\,\text{(mm day}^{-1})^{-1}]$. SWF contours are plotted at −9, −6, −3, −2, −1, −0.5, 0.5, 1, 2, 3, 6, and 9 $\text{W m}^{-2}\,\text{(mm day}^{-1})^{-1}$.

anomalies are mainly composed of SWF (contours in Figs. 3a,c,d) and LHF (contours in Figs. 4a,c,d). The SWF variations are related to changes in cloudiness associated with the MJO. The LHF variations are mainly modulated by changes in wind speeds with contributions from the zonal wind anomalies as noted in many MJO studies (e.g., Flatau et al. 1997; Woolnough et al. 2000; Hendon 2000; Inness et al. 2003). As to be discussed later in section 3c, our analysis shows that meridional wind anomalies also have significant contributions to the LHF variations.

In summary, the MJO, in terms of its propagation, amplitude, and periodicity, in general, is realistically simulated by CFSv2 with the RAS convection. The model horizontal resolution change from spectral T126 to T62 in the atmosphere and from 0.5° × 0.5° to 1° × 1° in the ocean is found to exert negligible effects on the representation of the MJO, particularly in regard to its eastward propagation. The MJO-related relationships between convection, surface fluxes, and SST are overall consistent with previous observational diagnoses (e.g., Krishnamurti et al. 1988; Shinoda et al. 1998; Woolnough et al. 2000) and generally follow the ASCII mechanism for the intraseasonal oscillation proposed by Flatau et al. (1997).

b. *The role of SST feedback in simulating MJO propagation*

Considering the comparable level of fidelity in simulating the MJO by CFSv2L_RAS and CFSv2_RAS as demonstrated above, and for faster turnover, CFSv2L_RAS is used for further experiments to explore the role

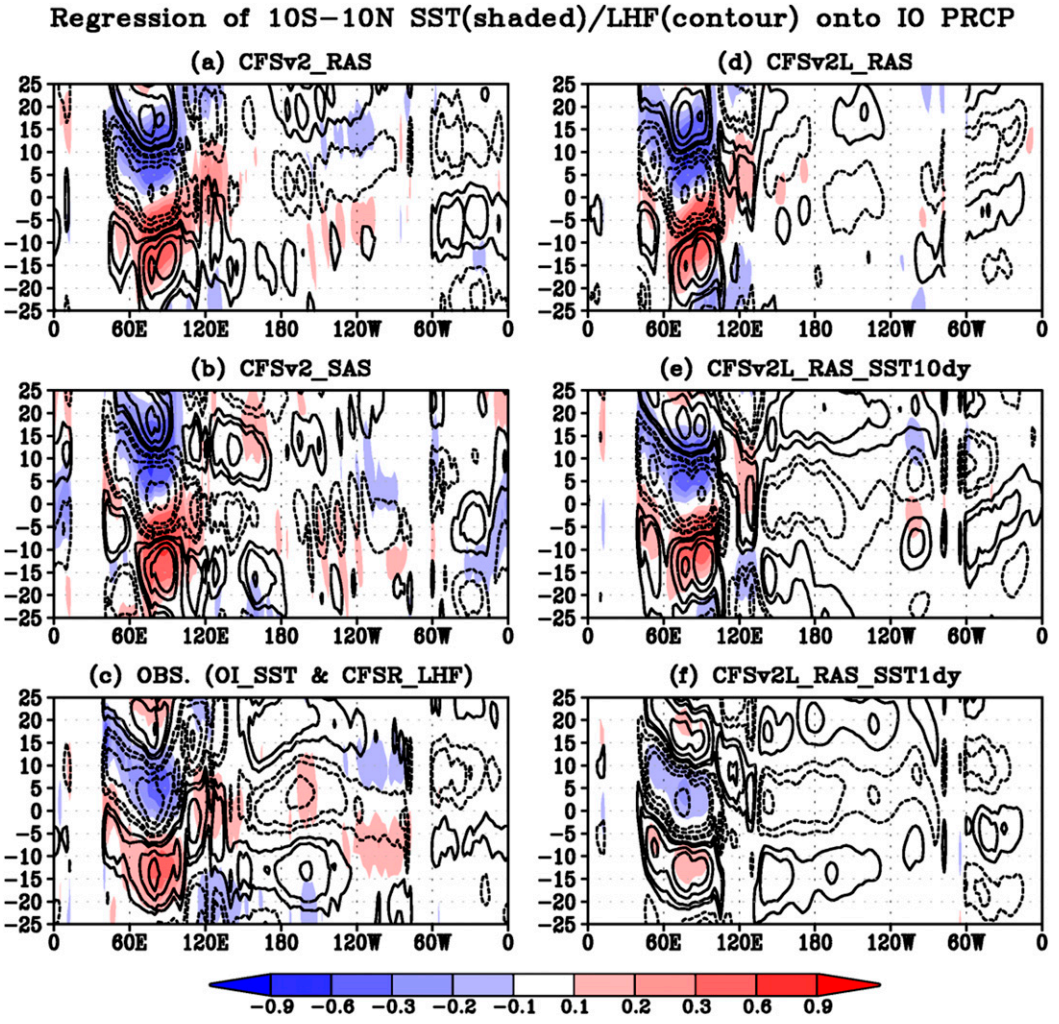

FIG. 4. As in Fig. 3, but for contours for surface downward LHF anomalies [W m^2 (mm day^{-1})$^{-1}$]. LHF contours are plotted at −9, −6, −3, −2, −1, −0.5, 0.5, 1, 2, 3, 6, and 9 W m^{-2} (mm day^{-1})$^{-1}$.

of SST feedback in simulating the MJO propagation. In particular, two experiments (i.e., CFSv2L_RAS_SST1dy and CFSv2L_RAS_SST10dy; see Table 1) are done with model SSTs nudged to the CFSv2L_RAS climatological state. The rationale behind the SST-nudged experiments is as follows: If the MJO is purely a result of internal atmospheric dynamics, the two nudged experiments should capture similar MJO features as the free run (i.e., CFSv2L_RAS). However, if substantial differences exist, it will indicate that SST feedback plays a role.

The diagnoses of the mean states suggest that the mean biases in SST, the low-level zonal wind, and precipitation are almost the same in two SST-nudged simulations and CFSv2L_RAS (figures not shown), which is to be expected from the experimental design. However, weakening the air–sea coupling strength has a clear reduction in the intraseasonal variance of 850-hPa zonal wind and precipitation over both the Indian Ocean and the western Pacific (figures not shown); hinting that SST feedback might be important in the MJO evolution. Also, the variance decrease is more significant in the western Pacific than in the Indian Ocean, suggesting that air–sea coupling might be more important for sustaining the MJO amplitude over the western Pacific.

Regarding the simulation of MJO propagation, SST feedback is found to play a critical role. For LHF, its variations over the Indian Ocean and the western Pacific exhibit many similar features in CFSv2L_RAS_SST10dy (contours in Fig. 4e) and CFSv2L_RAS_SST1dy (contours in Fig. 4f) as in CFSv2L_RAS (contours in Fig. 4d). For example, coincident with the precipitation over the Indian Ocean, there are positive LHF anomalies to the east of the precipitation center, which

are thought to be important for warm SST there and induce the convection to move eastward (Flatau et al. 1997). The similarity is because the MJO-related LHF variations are dominated by the wind speed variations (detailed analyses to be presented in section 3c), and the winds mainly change as a Gill-type response to the heating in the Indian Ocean.

For SWF (contours in Figs. 3d–f), its variations again highly resemble their respective patterns in precipitation (color shading in Figs. 2d–f), because of the associated changes in cloudiness. In particular, for both precipitation and SWF anomalies, while they exhibit well-defined eastward propagation in CFSv2L_RAS (Figs. 2d and 3d) as in reality (color shading in Fig. 2c and contours in Fig. 3c), such propagation seems absent as the nudging strength is as large as $O(1)\,\mathrm{day}^{-1}$ (color shading in Fig. 2f and contours in Fig. 3f); instead, a standing component is more evident. Furthermore, while precipitation and SWF anomalies could penetrate through the date line in CFSv2L_RAS (Figs. 2d and 3d) as in observations (Figs. 2c and 3c), they are generally confined to the west of the western Pacific in CFSv2L_RAS_SST1dy (Figs. 2f and 3f). The feature is consistent with the intraseasonal variance distribution that shows clearly weakened variance over the western Pacific as a result of the strong nudging (figures not shown).

The unrealistic intraseasonal features of precipitation (and SWF) simulated by CFSv2L_RAS_SST1dy could be explained by the associated variabilities in SST (contours in Fig. 2f). As a result of strong nudging to the climatological state [i.e., $O(1)\,\mathrm{day}^{-1}$], SST exhibits much weaker intraseasonal variations than that in CFSv2L_RAS (Fig. 2d vs Fig. 2f). Outside the Indian Ocean, there are no clear SST intraseasonal variations in CFSv2L_RAS_SST1dy (contours in Fig. 2f). Without the corresponding warm SST forcing, the overlaying atmosphere will be more stable, hindering convective activity, which is evidenced by low precipitation variations between 140°E and 180°. Because of the lower variability in precipitation, zonal winds also exhibit lower intraseasonal variations (contours in Fig. 1f). When the nudging strength is weakened to $O(10)\,\mathrm{day}^{-1}$ (i.e., CFSv2L_RAS_SST10dy), the SST intraseasonal variations become stronger, as expected (contours in Fig. 2e). Consistently, more convection is invoked to the east of 140°E, and precipitation exhibits some level of eastward propagation (color shading in Fig. 2e), but the eastward propagation is still weaker than in CFSv2L_RAS (color shading in Fig. 2d).

Overall, the two SST nudging experiments based on CFSv2L_RAS suggest that SST feedback is critical in maintaining MJO propagation in the model. However, one could ask whether including the SST feedback alone in a coupled atmosphere–ocean model is sufficient for the simulation of the eastward propagation across the Maritime Continent, and if not, what processes are responsible for the unsuccessful simulation. These questions are addressed in the next subsection by comparing two coupled simulations with contrasting levels of fidelity in representing the MJO propagation.

c. *The role of convection schemes in the MJO simulations and processes contributing to favorable SSTs for MJO propagation*

In this part, the sensitivity of MJO simulations to convection schemes is first explored by comparing CFSv2_SAS with CFSv2_RAS. Then, we diagnose physical processes that explain contrasting levels of fidelity in representing the MJO propagation between them.

It should be noted that CFSv2_SAS corresponds to the standard version of CFSv2 (Saha et al. 2014), in which the MJO has been evaluated in terms of simulations and predictions (Weaver et al. 2011; Wang et al. 2014). It has been found that in CFSv2_SAS (Saha et al. 2014), the simulated MJO propagates slower than the observed, with difficulties traversing the Maritime Continent into the western Pacific (Weaver et al. 2011). Consistent with experiments based on CFSv1 (Seo and Wang 2010) and the atmospheric component of CFSv2 (Wang et al. 2015), our experiments suggest that the MJO propagation in CFSv2 is clearly better represented by replacing the SAS convection scheme (Pan and Wu 1995) with RAS (Moorthi and Suarez 1992, 1999). In particular, in CFSv2_RAS (Fig. 1a), the simulated MJO propagates realistically eastward across the Eastern Hemisphere at a speed of around $4\,\mathrm{m\,s}^{-1}$, and the zonal wind anomalies lag behind the precipitation anomalies by about 5–7 days, both resembling the observed features (Fig. 1c). In contrast, the intraseasonal precipitation anomalies in CFSv2_SAS clearly stop propagating when encountering the Maritime Continent (color shading in Fig. 1b) even though the zonal wind anomalies, as a Gill-type response to heating in the Indian Ocean, propagate farther and cross the date line. The MJO propagation bias is also evident in most coupled models in which SST feedback has been included (e.g., Jiang et al. 2015). Therefore, it can be concluded that the inclusion of SST feedback alone in coupled models is not sufficient for maintaining the MJO eastward propagation across the Maritime Continent.

In fact, despite of SST feedback being included in both CFSv2_RAS and CFSv2_SAS, quite different intraseasonal SST anomalies occur between them. In CFSv2_RAS (Fig. 2a), coincident with the precipitation in the Indian Ocean, warm SST anomalies appear in the

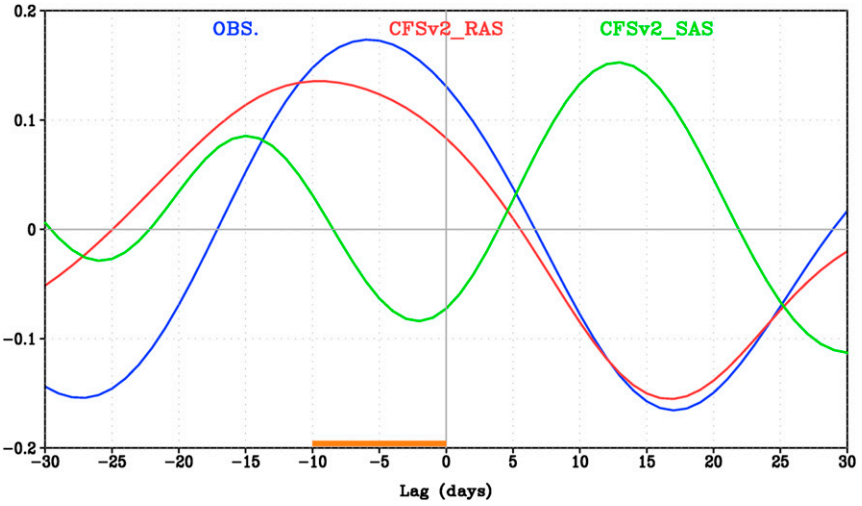

FIG. 5. November–April correlations between the intraseasonal (20–100-day filtered) precipitation anomalies over the Indian Ocean (10°S–10°N, 70°–100°E) and the intraseasonal LHF anomalies over 10°S–10°N, 120°–140°E for observations (CMORPH precipitation and CFSR heat flux; blue curves), CFSv2_RAS (red curves), and CFSv2_SAS (green curves).

western Pacific, as in observations (Fig. 2c). According to the ASCII mechanism (Flatau et al. 1997), the warm SST anomalies favor the eastward propagation of convection, traversing the Maritime Continent. However, in CFSv2_SAS, intraseasonal SST anomalies are generally confined within the Indian Ocean, and well-organized warm SST anomalies are absent in the western Pacific (contours in Fig. 2b), resulting in an unfavorable condition in the western Pacific for convection development and thus preventing the eastward propagation from the Indian Ocean.

Further diagnoses suggest that between two important factors (i.e., SWF and LHF) for the intraseasonal SST variations in the western Pacific, LHF is the dominant one for the difference between CFSv2_RAS and CFSv2_SAS. For SWF, in CFSv2_RAS (Fig. 3a), CFSv2_SAS (Fig. 3b), and observations (Fig. 3c), the western Pacific Ocean is all generally forced by positive SWF anomalies at the lag times from −10 to 0 days, which could drive warm SST anomalies locally. However, for LHF in the western Pacific ocean, CFSv2_SAS (Fig. 4b) is very different from CFSv2_RAS (Fig. 4a) and observations (Fig. 4c). In CFSv2_RAS and observations, positive LHF anomalies are evident in the western Pacific at the lag times from −10 to 0 days, which will reinforce the SWF effect on SST, resulting in local warm anomalies (color shading in Figs. 4a,c) coincident with precipitation in the Indian Ocean. In contrast, in CFSv2_SAS (Fig. 4b), for the same lag times, negative LHF anomalies are present, which will offset the SWF effect and favor near-normal SST condition over the region (color shading in Fig. 4b). The contrasting LHF difference between CFSv2_SAS and CFSv2_RAS or observations is more evident in Fig. 5, which calculates the lead–lag correlations between the intraseasonal precipitation anomalies over the Indian Ocean and the intraseasonal LHF anomalies over 10°S–10°N, 120°–140°E for boreal winter. It is clear that, over the lag time range from −15 to 30 days, the correlations in CFSv2_RAS are generally in-phase with the observed, but they are almost in an opposite phase with those in CFSv2_SAS (Fig. 5). Particularly, LHF has opposite signs between CFSv2_SAS and CFSv2_RAS or observations at the lag time from −10 to 0 days, which accumulatively contributes the SST anomalies at the 0-lag time.

To further explore factors influencing the intraseasonal LHF anomalies, we recalculate LHF based on the bulk formula with associated physical variables. By omitting the parameters that are nearly constant, LHF is calculated to the first order as follows:

$$\mathrm{LHF} \sim w(q_a - q_s), \tag{1}$$

where w is the 10-m wind speed, q_a is the 2-m specific humidity, and q_s is the saturation specific humidity at the ocean surface. By repeating Fig. 5 but using the recalculated LHF based on Eq. (1), the new lead–lag correlations (figures not shown, but the lead–lag regressions are shown in Fig. 6 as black curves) are found almost identical to those in Fig. 5 for both model simulations and observations, providing a justification for our LHF calculations.

According to Eq. (1), the intraseasonal LHF anomalies could be decomposed as follows:

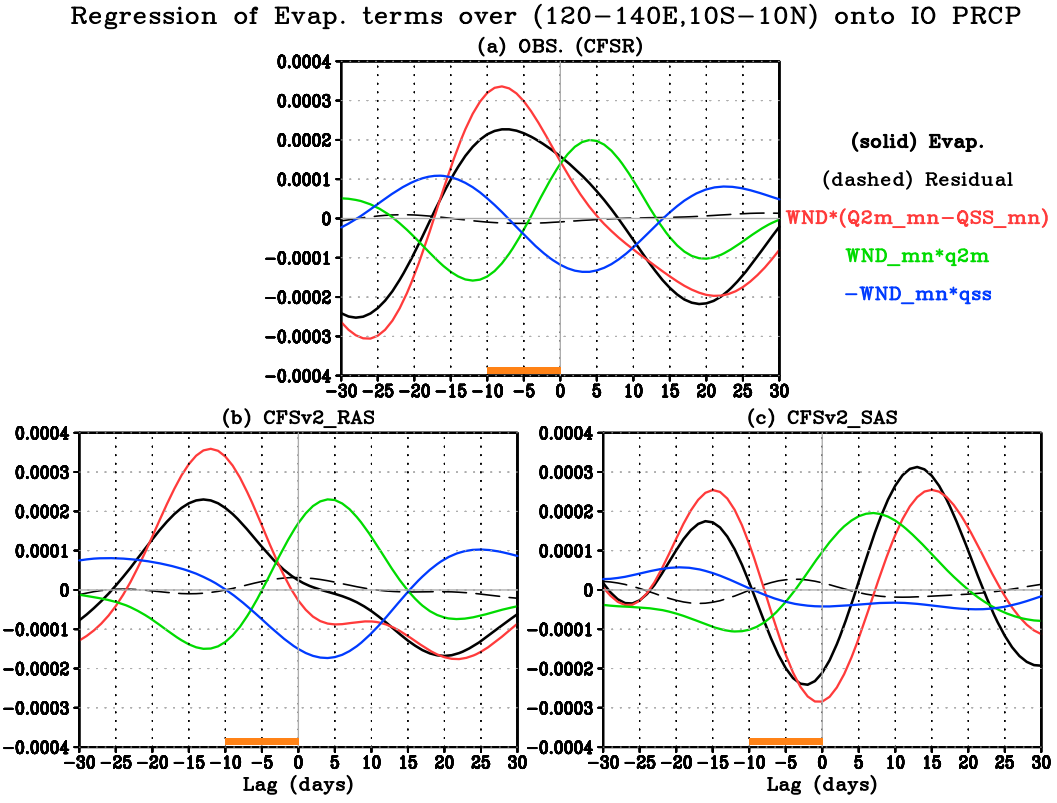

FIG. 6. November–April lead–lag regressions of different terms affecting the intraseasonal LHF anomalies (averaged over 10°S–10°N, 120°–140°E) against the Indian Ocean precipitation (10°S–10°N, 70°–100°E) for (a) observation (CFSR), (b) CFSv2_RAS, and (c) CFSv2_SAS [m s^{-1} (mm day^{-1})$^{-1}$]. The solid black curves are for δLHF (corresponding to curves in Fig. 5), with the red, green, and blue curves for $\delta w(\overline{q}_a - \overline{q}_s)$, $\overline{w}\delta q_a$, and $-\overline{w}\delta q_s$, respectively. The dashed curves are for the residual term in Eq. (2).

$$\delta\mathrm{LHF} \sim \delta w(\overline{q}_a - \overline{q}_s) + \overline{w}(\delta q_a - \delta q_s) + \varepsilon, \qquad (2)$$

where δ means the intraseasonal (20–100-day filtered) component, an overbar denotes the climatological mean during November–April, and ε is the residual term (i.e., the nonlinear term, which is the product of anomalous wind speeds and anomalous near-surface vertical gradients of moisture). Figure 6 presents the lead–lag regressions of δLHF, $\delta w(\overline{q}_a - \overline{q}_s)$, $\overline{w}\delta q_a$, $-\overline{w}\delta q_s$, and ε against the intraseasonal precipitation anomalies over the Indian Ocean for boreal winter. It is clear that, in model simulations and observations, the nonlinear term ε is negligibly small in association with the MJO (dashed curves in Fig. 6). Also, while the regressions with $\overline{w}\delta q_a$ (green curves in Fig. 6) and $-\overline{w}\delta q_s$ (blue curves in Fig. 6) are comparable in magnitude in observations and two model simulations, they are generally in opposite phase and cancel each other at the lag times from −30 to 30 days. As a result, the combined contributions of $\overline{w}\delta q_a$ and $-\overline{w}\delta q_s$ in δLHF are also generally small. In contrast, for observations and two model simulations, the regressions with the term $\delta w(\overline{q}_a - \overline{q}_s)$ (red curves in Fig. 6) are highly correlated with those about δLHF, which suggests that the intraseasonal LHF anomalies are mostly controlled by the product of anomalous wind speeds and mean near-surface vertical gradients of moisture [i.e., $\delta w(\overline{q}_a - \overline{q}_s)$].

Furthermore, it is encouraging to note that CFSv2 with the RAS convection not only realistically captures the lead–lag relationship of LHF with the Indian Ocean precipitation, but those about the decomposed terms associated with LHF are also realistically represented. For example, in observations, the product of mean wind speeds and anomalous near-surface vertical gradients of moisture (i.e., $-\overline{w}\delta q_s$; green curve in Fig. 6a) over 10°S–10°N, 120°–140°E, is featured by a peak of positive (negative) correlation with the precipitation in the Indian Ocean at the lag time of around 4 (−12) days, which is also captured by CFSv2_RAS (green curve in Fig. 6b). In fact, this feature also seems to be captured by CFSv2_SAS at a certain level (green curve in Fig. 6c). However, for the most important term for LHF, $\delta w(\overline{q}_a - \overline{q}_s)$ (red

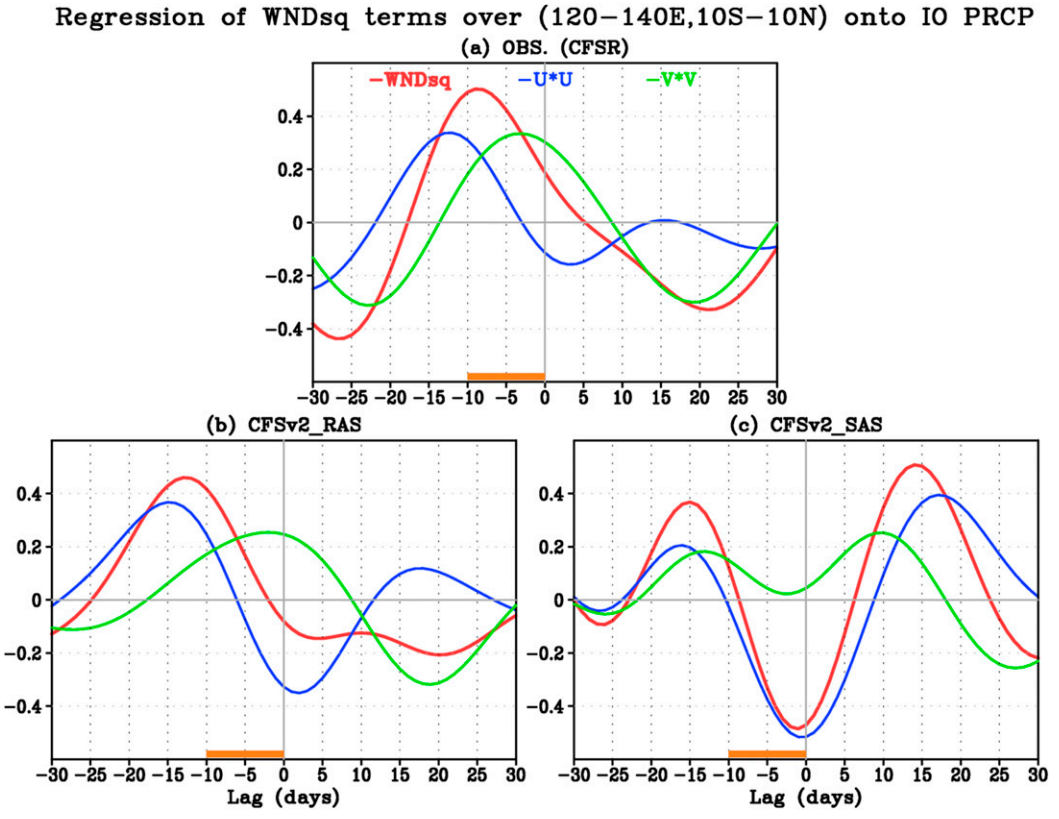

FIG. 7. November–April lead–lag regressions of the intraseasonal w^2, u^2, and v^2 anomalies (averaged over 10°S–10°N, 120°–140°E) against the Indian Ocean precipitation (10°S–10°N, 70°–100°E) for (a) observation (CFSR), (b) CFSv2_RAS, and (c) CFSv2_SAS. The red curves are for $-w^2$ (corresponding to red curves in Fig. 6), and the blue (green) curves are for $-u^2$ ($-v^2$) [$(\mathrm{m\,s^{-1}})^2$ $(\mathrm{mm\,day^{-1}})^{-1}$]. Note that regressions are calculated for the opposite sign of w^2, u^2, and v^2, which is to coincide with the sign of surface heat flux into the ocean.

curves in Fig. 6), a remarkable difference is evident between CFSv2_SAS and CFSv2_RAS or observations. Particularly, in association with intraseasonal SST anomalies over the western Pacific at the 0-day lag, $\delta w(\overline{q}_a - \overline{q}_s)$ makes a positive contribution in CFSv2_RAS and observations but a negative contribution in CFSv2_SAS, which can be seen from their integrated effects during the lag times from −10 to 0 days. Therefore, it is concluded that it is the difference in simulated wind speeds that plays a major role in the difference of intraseasonal LHF variations over the western Pacific, which results in a substantial difference in local SST conditions between CFSv2_SAS and CFSv2_RAS.

As a further step in diagnostics, we are interested to know the contribution from each of the wind components (i.e., the zonal and meridional winds). In Fig. 7, we calculate the lead–lag regressions of intraseasonal w^2, u^2, and v^2 anomalies (averaged over 10°S–10°N, 120°–140°E) against the intraseasonal precipitation anomalies over the Indian Ocean for boreal winter, where w^2 is the square of the magnitude of the 10-m wind speed, and u^2 (v^2) is the square of the 10-m zonal (meridional) wind component. Note that the regressions in Fig. 7 have been multiplied with a minus sign to mimic the sign of surface heat flux into the ocean. Comparing CFSv2_RAS (Fig. 7b) and observations (Fig. 7a), the lead–lag regressions are again generally in the same phase for intraseasonal w^2, u^2, and v^2 anomalies.

We next focus on the lag times close to 0 when dramatically different SST conditions appear in the western Pacific between CFSv2_SAS and CFSv2_RAS or observations (Fig. 2). In CFSv2_RAS and the observation (Figs. 7a,b), the total wind speed (red curves) is weakened for most of the lag time after day −20 and before the 0-day lag, and the change in both the zonal and meridional components contribute to the total wind speed weakening. The regression for $-u^2$ (blue curves) becomes positive after the lag time of day −22 in the observation and day −29 in CFSv2_RAS, increases to a positive maximum value from days −13 to −14, and then decreases and reaches a negative minimum value around day 2. The regression for $-v^2$ increases from

zero around day −14 in the observation and day −17 in CFSv2_RAS, reaching a positive maximum value around day −3. The net effect of the two wind components in CFSv2_RAS and observations is a positive regression for $-w^2$, corresponding to weakening of total wind speed, during most of the lag time from day −20 to 0. The weakening of the wind speed is largely from the change in the zonal component before day −9. After day 0, the weakening of the wind speed is dominated by the change in the meridional wind.

In contrast, in CFSv2_SAS (Fig. 7c), the wind speed weakens before day −9, after which the wind speed becomes stronger, and the contribution from the meridional component is much smaller compared to that in the observation and CFSv2_RAS. Both u^2 and v^2 in CFSv2_SAS are quite different from those in the CFSv2_RAS and observation. For u^2 (blue curve in Fig. 7c), the negative regression values for $-u^2$ before the 0-day lag starts at day −10 in CFSv2_SAS, much earlier than that in the observation (day −3) and CFSv2_RAS (day −6), and the amplitude of the negative regression values for $-u^2$ in CFSv2_SAS is much larger than in the observation and CFSv2_RAS. For v^2 (green curve in Fig. 7c), the amplitude of the positive regression in CFSv2_SAS is quite small, with a local minimum at the lag time around day −3 in contrast to a local maximum in CFSv2_RAS and observations. The weak positive regression for the meridional component and the large negative regression for the zonal component in CFSv2_SAS result in net strengthened wind over 10°S–10°N, 120°–140°E prior to the 0-lag time, which is contrary to the weakened total wind speed because of the reduced amplitude of meridional velocity in the CFSv2_RAS and observation. It should be noted that the difference of the intraseasonal wind anomalies between CFSv2_SAS and CFSv2_RAS cannot be attributed to the difference in climatological state as the climatological surface winds are, overall, similar between the two simulations (figures not shown).

The difference of u^2 and v^2 between two simulations is also evident in Fig. 8, which demonstrates the spatial patterns of above regressions averaged over the lag times from −10 to 0 days. East of 120°E, in CFSv2_RAS, similar to observations, $-u^2$ is featured by positive regressions coherent with negative regressions, but in CFSv2_SAS, it is clearly dominated by positive regressions. Also, while $-v^2$ shows uniform positive regressions east of 120°E in CFSv2_RAS and observations, for CFAv2_SAS, it has clear negative regressions.

To summarize, the coupled experiments with different convection schemes indicate that air–sea coupling alone cannot maintain the MJO eastward propagation across the Maritime Continent, but favorable preconditioning of SSTs must be realistically developed in models. Further, for the development of such SST conditions, not only the zonal surface winds should be realistically represented, as highlighted in previous MJO studies (e.g., Flatau et al. 1997; Hendon 2000; Inness and Slingo 2003, Liess et al. 2004; Zhang 2005), but the meridional component is also equally important, a fact that has been ignored in most MJO studies.

4. Conclusions and discussion

In this study, we contribute to the continuing efforts to understand the causes for problems in the MJO simulations, particularly in its eastward propagation. In particular, a series of coupled simulations are conducted based on the NCEP Climate Forecast System, version 2 (CFSv2) to explore the sensitivity of the MJO simulations to changes in model configurations, including horizontal resolutions, air–sea coupling, and convection schemes. The model results are also compared with observations to verify their fidelity.

First, two simulations with different horizontal resolutions are compared, which are based on the RAS convection scheme. It is found that the MJO, in terms of its propagation, amplitude, and periodicity, is generally realistically simulated. Furthermore, the model horizontal resolution change from T126 for the atmosphere and 0.5° × 0.5° for the ocean to T62 for the atmosphere and 1° × 1° for the ocean exerts negligible influence on the representation of the MJO. In addition, the MJO-related relationships between convection, surface fluxes, and SST are overall consistent with previous observational diagnoses (e.g., Krishnamurti et al. 1988; Shinoda et al. 1998; Woolnough et al. 2000) and generally follow the ASCII mechanism for the intraseasonal oscillation proposed by Flatau et al. (1997).

Further, based on the CFSv2 with lower resolution (CFSv2L), two more experiments were performed with model SSTs nudged to model climatologies at the restoring time scales of 10 days and 1 day, respectively. It is found that weakening the air–sea coupling strength significantly degraded MJO propagation, suggesting the critical role of SST feedback in maintaining MJO propagation.

Last, the sensitivity to convection parameterization is explored by comparing two CFSv2 simulations with the RAS and SAS convection parameterization schemes. Analyses indicated that while CFSv2 with RAS simulates the MJO quite realistically, the MJO-related convection in the simulation with SAS could not propagate eastward across the Maritime Continent. It suggests that air–sea coupling alone cannot maintain the MJO eastward propagation across the Maritime

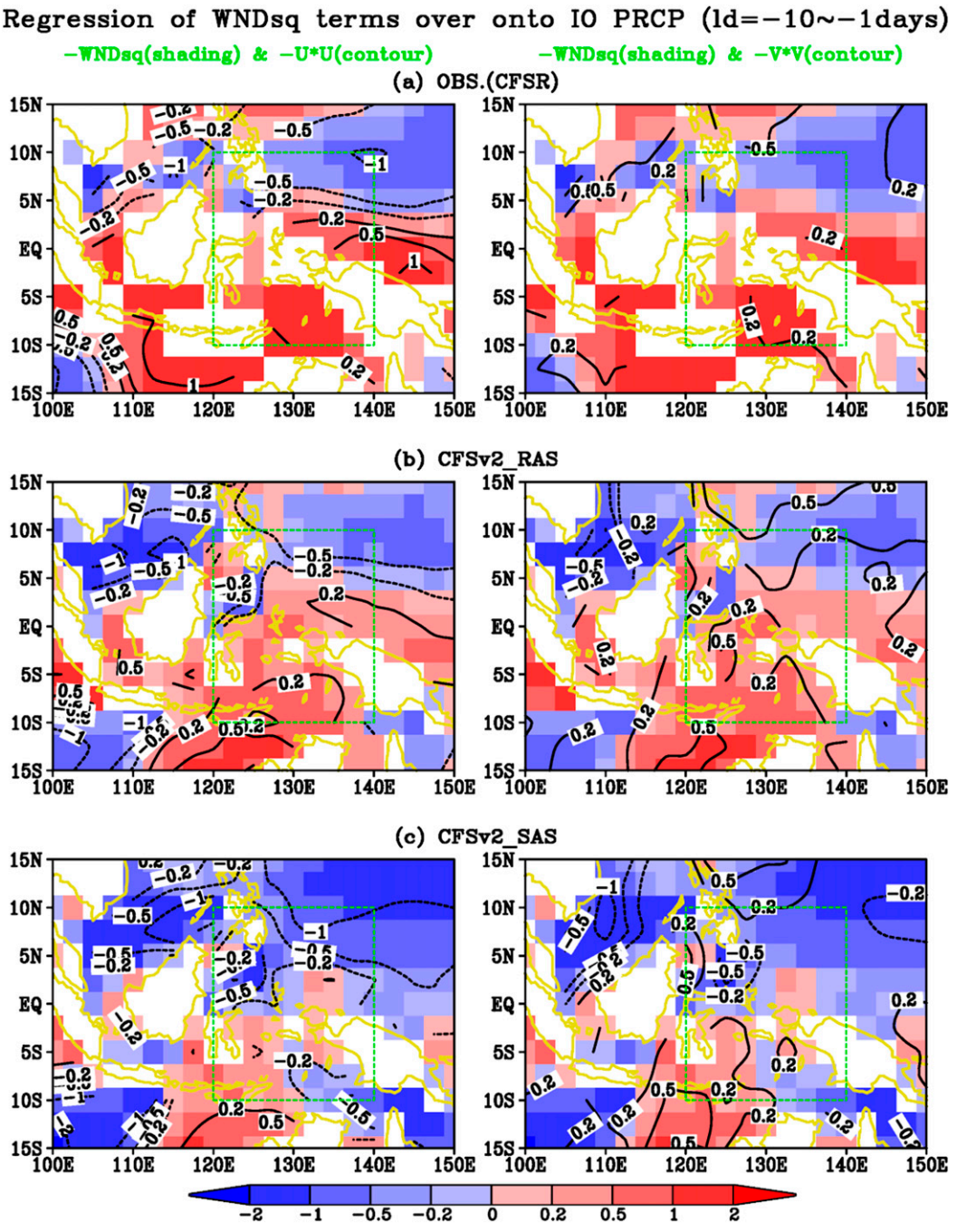

FIG. 8. November–April regressions of the intraseasonal w^2, u^2, and v^2 anomalies against the Indian Ocean precipitation (10°S–10°N, 70°–100°E) for (a) observation (CFSR), (b) CFSv2_RAS, and (c) CFSv2_SAS. The regressions are shown as averages over from −10 to −1 days when precipitation lags the formers. The left (right) column is for $-w^2$ and $-u^2$ ($-v^2$), with the former color shaded and the latter contoured [$(\mathrm{m\,s^{-1}})^2$ $(\mathrm{mm\,day^{-1}})^{-1}$].

Continent. Further analyses indicated that favorable SST conditions must be realistically developed in models. In both observations and the simulation with RAS, warm SST anomalies corresponding to precipitation in the Indian Ocean were present to the east of the Maritime Continent. This SST signal, however, was absent in the simulation based on SAS. The difference in surface latent heat fluxes was further identified as the major factor resulting in the SST difference.

Detailed diagnoses of the latent heat flux suggest that, in both observations and the RAS simulation, east of the Maritime Continent, the latent heat flux intraseasonal variability was generally controlled by surface wind speeds. Prior to the local warm SST anomalies, mostly as a result of weakened meridional surface wind, the surface wind becomes weaker than normal, which leads to less latent heat flux out of the ocean, accumulatively responsible for the late warm SST anomalies. On the other hand, as a result of unrealistic representation of both zonal and meridional winds in the SAS simulation, the surface wind became stronger than normal, resulting in more latent heat flux out of the ocean. When working together with the surface solar shortwave radiation flux, near-normal SST condition is forced to the east of the Maritime Continent. As a result, the MJO-related convection stopped propagating farther eastward in the SAS simulation.

It is worthwhile to highlight that, in the development of favorable SST conditions for the MJO propagation, not only the zonal surface winds should be realistically represented as noted in previous MJO studies (e.g., Flatau et al. 1997; Hendon 2000; Inness and Slingo 2003, Liess et al. 2004; Zhang 2005), but the meridional component is also equally important. This factor has been largely neglected in most of the previous MJO studies. Further studies are required to understand how the surface winds are affected by the different convection schemes, which represents the next challenge.

It is also noted that some studies (e.g., the moisture-mode theory) suggested that the horizontal advection of moisture is an important factor for MJO propagation (Kim et al. 2014). Thus, the moisture-mode theory is another aspect that may help understand the MJO differences simulated by two convection schemes, but it is not the focus of the paper, which focuses on the ocean surface impact. In addition, an analysis of mixed layer depth (MLD; figures not shown) in CFSv2L_RAS indicates that MLD nearly varies in phase with intraseasonal SST variations, with shallow MLD accompanying warm SST. Considering that as a response to fixed heat fluxes, shallower MLD will result in warmer SST, the warm SST east of 120°E might involve upper-ocean processes, which will also be explored in the future.

Acknowledgments. We thank NOAA's Climate Program Office for their support through the Modeling, Analysis, Predictions, and Projections (MAPP) and Climate Variability and Predictability (CVP) programs. We greatly appreciate the helpful internal reviews by Drs. Hui Wang and Steve Baxter.

REFERENCES

Arakawa, A., and W. H. Schubert, 1974: Interaction of a cumulus cloud ensemble with the large-scale environment, Part I. *J. Atmos. Sci.*, **31**, 674–704, doi:10.1175/1520-0469(1974)031<0674:IOACCE>2.0.CO;2.

Bechtold, P., M. Köhler, T. Jung, F. Doblas-Reyes, M. Leutbecher, M. J. Rodwell, F. Vitart, and G. Balsamo, 2008: Advances in simulating atmospheric variability with the ECMWF model: From synoptic to decadal time-scales. *Quart. J. Roy. Meteor. Soc.*, **134**, 1337–1351, doi:10.1002/qj.289.

Crueger, T., B. Stevens, and R. Brokopf, 2013: The Madden–Julian oscillation in ECHAM6 and the introduction of an objective MJO metric. *J. Climate*, **26**, 3241–3257, doi:10.1175/JCLI-D-12-00413.1.

DeMott, C. A., N. P. Klingaman, and S. J. Woolnough, 2015: Atmosphere–ocean coupled processes in the Madden–Julian oscillation. *Rev. Geophys.*, **53**, 1099–1154, doi:10.1002/2014RG000478.

Flatau, M., P. J. Flatau, P. Phoebus, and P. P. Niiler, 1997: The feedback between equatorial convection and local radiative and evaporative processes: The implications for intraseasonal oscillations. *J. Atmos. Sci.*, **54**, 2373–2386, doi:10.1175/1520-0469(1997)054<2373:TFBECA>2.0.CO;2.

Fu, X., B. Yang, Q. Bao, and B. Wang, 2008: Sea surface temperature feedback extends the predictability of tropical intraseasonal oscillation. *Mon. Wea. Rev.*, **136**, 577–597, doi:10.1175/2007MWR2172.1.

Grell, G. A., 1993: Prognostic evaluation of assumptions used by cumulus parameterization. *Mon. Wea. Rev.*, **121**, 764–787, doi:10.1175/1520-0493(1993)121<0764:PEOAUB>2.0.CO;2.

Hendon, H. H., 2000: Impact of air–sea coupling on the Madden–Julian oscillation in a general circulation model. *J. Atmos. Sci.*, **57**, 3939–3952, doi:10.1175/1520-0469(2001)058<3939:IOASCO>2.0.CO;2.

Hung, M.-P., J.-L. Lin, W. Wang, D. Kim, T. Shinoda, and S. J. Weaver, 2013: MJO and convectively coupled equatorial waves simulated by CMIP5 climate models. *J. Climate*, **26**, 6185–6214, doi:10.1175/JCLI-D-12-00541.1.

Inness, P. M., and J. M. Slingo, 2003: Simulation of the Madden–Julian oscillation in a coupled general circulation model. Part I: Comparison with observations and an atmosphere-only GCM. *J. Climate*, **16**, 345–364, doi:10.1175/1520-0442(2003)016<0345:SOTMJO>2.0.CO;2.

——, and ——, 2006: The interaction of the Madden–Julian oscillation with the Maritime Continent in a GCM. *Quart. J. Roy. Meteor. Soc.*, **132**, 1645–1667, doi:10.1256/qj.05.102.

——, ——, E. Guilyardi, and J. Cole, 2003: Simulation of the Madden–Julian oscillation in a coupled general circulation model. Part II: The role of the basic state. *J. Climate*, **16**, 365–382, doi:10.1175/1520-0442(2003)016<0365:SOTMJO>2.0.CO;2.

Jiang, X., and Coauthors, 2015: Vertical structure and physical processes of the Madden–Julian oscillation: Exploring key model physics in climate simulations. *J. Geophys. Res. Atmos.*, **120**, 4718–4748, doi:10.1002/2014JD022375.

Joyce, R. J., J. E. Janowiak, P. A. Arkin, and P. Xie, 2004: CMORPH: A method that produces global precipitation estimates from passive microwave and infrared data at high spatial and temporal resolution. *J. Hydrometeor.*, **5**, 487–503, doi:10.1175/1525-7541(2004)005<0487:CAMTPG>2.0.CO;2.

Kemball-Cook, S., B. Wang, and X. Fu, 2002: Simulation of the intraseasonal oscillation in the ECHAM-4 model: The impact of coupling with an ocean model. *J. Atmos. Sci.*, **59**, 1433–1453, doi:10.1175/1520-0469(2002)059<1433:SOTIOI>2.0.CO;2.

Kim, D., J.-S. Kug, and A. H. Sobel, 2014: Propagating versus nonpropagating Madden–Julian oscillation events. *J. Climate*, **27**, 111–125, doi:10.1175/JCLI-D-13-00084.1.

Kim, H.-M., D. Kim, F. Vitart, V. E. Toma, J.-S. Kug, and P. J. Webster, 2016: MJO propagation across the Maritime Continent in the ECMWF ensemble prediction system. *J. Climate*, **29**, 3973–3988, doi:10.1175/JCLI-D-15-0862.1.

Krishnamurti, T. N., D. K. Oosterhof, and A. V. Metha, 1988: Air–sea interaction on the time scale of 30 to 50 days. *J. Atmos. Sci.*, **45**, 1304–1322, doi:10.1175/1520-0469(1988)045<1304:AIOTTS>2.0.CO;2.

Kumar, A., L. Zhang, and W. Wang, 2013: Sea surface temperature–precipitation relationship in different reanalyses. *Mon. Wea. Rev.*, **141**, 1118–1123, doi:10.1175/MWR-D-12-00214.1.

Liess, S., L. Bengtsson, and K. Arpe, 2004: The intraseasonal oscillation in ECHAM4 part I: Coupled to a comprehensive ocean model. *Climate Dyn.*, **22**, 653–669, doi:10.1007/s00382-004-0406-0.

Lin, J.-L., and Coauthors, 2006: Tropical intraseasonal variability in 14 IPCC AR4 climate models. Part I: Convective signals. *J. Climate*, **19**, 2665–2690, doi:10.1175/JCLI3735.1.

——, M.-I. Lee, D. Kim, I.-S. Kang, and D. M. W. Frierson, 2008: The impacts of convective parameterization and moisture triggering on AGCM-simulated convectively coupled equatorial waves. *J. Climate*, **21**, 883–909, doi:10.1175/2007JCLI1790.1.

Madden, R. A., and P. R. Julian, 1971: Detection of a 40–50 day oscillation in the zonal wind in the tropical Pacific. *J. Atmos. Sci.*, **28**, 702–708, doi:10.1175/1520-0469(1971)028<0702:DOADOI>2.0.CO;2.

Moorthi, S., and M. J. Suarez, 1992: Relaxed Arakawa–Schubert: A parameterization of moist convection for general circulation models. *Mon. Wea. Rev.*, **120**, 978–1002, doi:10.1175/1520-0493(1992)120<0978:RASAPO>2.0.CO;2.

——, and ——, 1999: Documentation of version 2 of relaxed Arakawa–Schubert cumulus parameterization with convective downdrafts. NOAA Tech. Note NWS/NCEP 99-01, 44 pp.

Pan, H.-L., and W.-S. Wu, 1995: Implementing a mass flux convection parameterization package for the NMC medium-range forecast model. NMC Tech. Note 409, 39 pp.

Pegion, K., and B. P. Kirtman, 2008: The impact of air–sea interactions on the predictability of the tropical intraseasonal oscillation. *J. Climate*, **21**, 5870–5886, doi:10.1175/2008JCLI2209.1.

Reynolds, R. W., T. M. Smith, C. Liu, D. B. Chelton, K. S. Casey, and M. G. Schlax, 2007: Daily high-resolution-blended analyses for sea surface temperature. *J. Climate*, **20**, 5473–5496, doi:10.1175/2007JCLI1824.1.

Saha, S., and Coauthors, 2010: The NCEP Climate Forecast System Reanalysis. *Bull. Amer. Meteor. Soc.*, **91**, 1015–1057, doi:10.1175/2010BAMS3001.1.

——, and Coauthors, 2014: The NCEP Climate Forecast System version 2. *J. Climate*, **27**, 2185–2208, doi:10.1175/JCLI-D-12-00823.1.

Schiemann, R., M.-E. Demory, M. S. Mizielinski, M. J. Roberts, L. C. Shaffrey, J. Strachan, and P. L. Vidale, 2014: The sensitivity of the tropical circulation and Maritime Continent precipitation to climate model resolution. *Climate Dyn.*, **42**, 2455–2468, doi:10.1007/s00382-013-1997-0.

Seo, K.-H., and W. Wang, 2010: The Madden–Julian oscillation simulated in the NCEP Climate Forecast System model: The importance of stratiform heating. *J. Climate*, **23**, 4770–4793, doi:10.1175/2010JCLI2983.1.

Shelly, A., P. Xavier, D. Copsey, T. Johns, J. M. Rodriguez, S. Milton, and N. Klingaman, 2014: Coupled versus uncoupled hindcast simulations of the Madden–Julian oscillation in the Year of Tropical Convection. *Geophys. Res. Lett.*, **41**, 5670–5677, doi:10.1002/2013GL059062.

Shinoda, T., H. H. Hendon, and J. Glick, 1998: Intraseasonal variability of surface fluxes and sea surface temperature in the tropical western Pacific and Indian Oceans. *J. Climate*, **11**, 1685–1702, doi:10.1175/1520-0442(1998)011<1685:IVOSFA>2.0.CO;2.

Slingo, J. M., and Coauthors, 1996: Intraseasonal oscillations in 15 atmospheric general circulation models: Results from an AMIP diagnostic subproject. *Climate Dyn.*, **12**, 325–357, doi:10.1007/BF00231106.

Tokioka, T., K. Yamazaki, A. Kitoh, and T. Ose, 1988: The equatorial 30–60 day oscillation and the Arakawa–Schubert penetrative cumulus parameterization. *J. Meteor. Soc. Japan*, **66**, 883–901. [Available online at https://www.jstage.jst.go.jp/article/jmsj1965/66/6/66_6_883/_pdf.]

Vitart, F., S. Woolnough, M. A. Balmaseda, and A. M. Tompkins, 2007: Monthly forecast of the Madden–Julian oscillation using a coupled GCM. *Mon. Wea. Rev.*, **135**, 2700–2715, doi:10.1175/MWR3415.1.

Waliser, D. E., K. M. Lau, and J.-H. Kim, 1999: The influence of coupled sea surface temperatures on the Madden–Julian oscillation: A model perturbation experiment. *J. Atmos. Sci.*, **56**, 333–358, doi:10.1175/1520-0469(1999)056<0333:TIOCSS>2.0.CO;2.

Wang, W., and M. E. Schlesinger, 1999: The dependence on convection parameterization of the tropical intraseasonal oscillation simulated by the UIUC 11-layer atmospheric GCM. *J. Climate*, **12**, 1423–1457, doi:10.1175/1520-0442(1999)012<1423:TDOCPO>2.0.CO;2.

——, M.-P. Hung, S. J. Weaver, A. Kumar, and X. Fu, 2014: MJO prediction in the NCEP Climate Forecast System version 2. *Climate Dyn.*, **42**, 2509–2520, doi:10.1007/s00382-013-1806-9.

——, A. Kumar, J. X. Fu, and M.-P. Hung, 2015: What is the role of the sea surface temperature uncertainty in the prediction of tropical convection associated with the MJO? *Mon. Wea. Rev.*, **143**, 3156–3175, doi:10.1175/MWR-D-14-00385.1.

Weaver, S. J., W. Wang, M. Chen, and A. Kumar, 2011: Representation of MJO variability in the NCEP Climate Forecast System. *J. Climate*, **24**, 4676–4694, doi:10.1175/2011JCLI4188.1.

Woolnough, S. J., J. M. Slingo, and B. J. Hoskins, 2000: The relationship between convection and sea surface temperature on intraseasonal timescales. *J. Climate*, **13**, 2086–2104, doi:10.1175/1520-0442(2000)013<2086:TRBCAS>2.0.CO;2.

Zhang, C., 2005: Madden–Julian oscillation. *Rev. Geophys.*, **43**, RG2003, doi:10.1029/2004RG000158.

——, M. Dong, S. Gualdi, H. H. Hendon, E. D. Maloney, A. Marshall, K. R. Sperber, and W. Wang, 2006: Simulations of the Madden–Julian oscillation in four pairs of coupled and uncoupled global models. *Climate Dyn.*, **27**, 573–592, doi:10.1007/s00382-006-0148-2.

Zhang, G. J., and M. Mu, 2005: Simulation of the Madden–Julian oscillation in the NCAR CCM3 using a revised Zhang–McFarlane convection parameterization scheme. *J. Climate*, **18**, 4046–4064, doi:10.1175/JCLI3508.1.